12

MEMS Gyroscopes for Consumer and Industrial Applications

Riccardo Antonello and Roberto Oboe
Dept. of Management and Engineering,
University of Padova - Vicenza branch
Italy

1. Introduction

The advent of MEMS (Micro-Electro-Mechanical-System) technology has enabled the development of miniaturized, low-cost, low-power sensors that are currently replacing their macroscopic scale equivalents in many traditional applications, covering industrial, automotive, biomedical, consumer applications, etc.

Competitiveness of MEMS sensors largely resides in the miniaturization and batch fabrication processes involved in their manufacture, which allow to cut down costs, size and power requirements of the final device. Moreover, miniaturization opens new perspectives and possibilities for the development of completely new class of sensors, where micro-scale phenomena are effectively pursued to achieve results that would be unfeasible at a macro-scale.

Several MEMS sensor typologies are either commercially available or have been presented in technical literature since the beginning of the microsystem technology more than 30 years ago. Pressure and acceleration sensors for the automotive industry have been among the first MEMS devices to be produced in large scale, and they have contributed to foster the further development of MEMS technology. Despite their maturity, these sensors are still dominating, with their sales volume, the market of silicon-based sensors. Recently, another micro-sensor that is becoming relevant in terms of sales volume, especially in the automotive and consumer electronics markets, is the angular rate sensor, or *gyroscope*.

Alongside with accelerometers, micromachined gyroscopes can be used in several applications that require an integrated solution for inertial sensing and motion processing problems (Söderkvist, 1994; Yazdi et al., 1998). In the automotive industry, they can be integrated in advanced safety systems for skid (e.g. ESC - *electronic stability control*) and roll-over (e.g. RSC - *roll-over stability control*) detection and prevention (tilt and yaw control) (Neul et al., 2007; Nonomura et al., 2006; Sparks et al., 1997; Voss et al., 1997), or they can be used in vehicle navigation systems, either as stand-alone or GPS (*Global Positioning System*)-assisted solutions (Brown, 2005; Noureldin et al., 2009). Other automotive applications include *anti-lock braking systems* (ABS), active suspension control for comfort riding and improved vehicle handling, and smart cruise control systems (Fleming, 2001; Seidel et al., 2002).

In consumer electronics, micromachined inertial sensors are used in *Optical Image Stabilization* (OIS) systems for cameras and camcorders (Sachs et al.), in dead reckoning personal

navigation systems (either stand-alone or integrated in cell-phones and PDAs, such as the Apple's *iPhone*, *iPad* and *iPod touch* (Apple, 2011)), in 3D-pointing devices such as the Nintendo Wii's game controller (*Wiimote*) with MotionPlus expansion (Nintendo, 2011), the Gyration air mice (Gyration, 2009) or the SCURRY glove-like input device (Kim et al., 2005), and virtual reality headsets. Industrial applications of MEMS inertial sensors may include integrated IMUs (*Inertial Measurement Units*) for AGVs (Automated Guided vehicles) (Microstrain, 2011), distribute sensing and monitoring of industrial plants, motion control of manipulators and machine tools, platform stabilization of heavy machineries, stabilization systems for mobile antennas, integrated inertial platforms for personal transportation systems (Segway, 2011), etc. Some biomedical applications have also been reported, including system for the gait-phase detection (Pappas et al., 2004), the ambulatory analysis of the human posture (Roetenberg et al., 2007), (Kawano et al., 2007) and the estimation of the stride length and walking velocity (Miyazaki, 1997).

To pioneer the commercialization of MEMS gyroscopes has been *Robert Bosch GmbH.*, which introduced the first MEMS gyroscope-based vehicle stability control system in 1998. Since then, many other manufacturers have embarked in the effort of producing and commercializing micromachined angular sensors, attracted by the market opportunities and the predicted sales volumes for MEMS gyros. A list of current manufacturers of MEMS gyros includes the followings (here reported in any specific order): *Analog Devices* (ADI), *Robert Bosch GmbH*, *Honeywell*, *Draper Laboratories*, *Silicon Sensing Systems* - SSS (BAE/*Sumitomo Precision Products*), *Invensense*, *MEMSense*, *BAE/AMI Semiconductors*, *ST Microelectronics*, *NEC-Tokin*, *Epson Toyocom*, *muRata*, *Systron Donner*, *Northrop Grumman*, *Goodrich Corp.*, *Melexis*, *SensoNor*, *IMEGO*, *Gyrooptics*, *Gladiator Technologies*. Even if most of them are direct competitors, their production is diversified in terms of addressed market segments (i.e. cost and performance of the sensor), technical specifications, fabrication technology, etc.

2. Operating principle of conventional and miniaturized gyroscopes

2.1 Conventional gyroscopes

Gyroscopes are sensors designed for measuring angular rotations about some specific axes with respect to inertial space. *Rate gyroscopes* measure a rotation rate (angular velocity), while *displacement gyroscopes* (also known as *whole-angle gyroscopes*) measure a rotation angle. They have been traditionally designed as either mechanical devices exploiting the conservation of the angular momentum stored in a spinning wheel, or as optical systems exploiting the Sagnac effect experienced by counter-propagating laser beams in a ring cavity or a fiber optic coil. Typical designs include:

- *Momentum wheel gyroscopes*: they consist of a spinning wheel mounted on a gimbal support, whose function is to isolate the wheel spin axis from rotations of the body on which the gyro is attached to. Because of the conservation of the angular momentum, the spin axis remains fixed during the body motion, and therefore the gimbal angles provide a measurement of the body angular displacement with respect to an inertial frame. A key design issue in momentum wheel gyroscope is the reduction of bearing friction, since it strongly affects the measurement drift. Friction reduction can be achieved with innovative suspension designs (e.g. gas bearings, electrostatic and magnetic suspensions, floated gyros, etc.) or by employing a slightly different mechanical design, such as in the *Dynamically Tuned Gyroscope* (DTG). In DTG, a rotor (momentum wheel) is attached to a motor shaft by means of a gimbal mechanism with flexible suspensions. As the rotor spins,

driven by the motor, the gimbal rotates without twisting the flexures only if the motor shaft is aligned with the rotor axis, otherwise the rotor starts fluttering and the flexures are twisted by gyroscopic precession torques. As a net effect, such torques produce a reduction of the equivalent stiffness of the flexures (softening effect); therefore, depending on the misalignment of the motor shaft and the rotor axis (i.e. the body attitude with respect to an inertial frame), there is a suitable rotor spin rate at which the equivalent stiffness of the flexures is nulled and the rotor is unrestrained. This properly tuned rotor spin rate provides an indirect measurement of the angular displacement.

- *Ring Laser Gyroscopes* (RLG): they consist of a polygonal closed gas cavity inside which two laser beams are propagated in opposite directions, namely clockwise (CW) and counterclockwise (CCW). After traveling along the whole cavity, the two beams meet at a return point and an interference pattern is obtained. The displacement between adjacent interference fringes is affected by the sensor rotation rate: this is a consequence of the Sagnac effect, namely the difference in the travel path length experienced by the two beams whenever the RLG undergoes a rotation whose axis is normal to the waveguide plane. Therefore, a measurement of the sensor angular velocity can be provided by measuring either the displacement shift of the interference fringes or, more commonly, the phase shift of the two beams (using a photodetector at the return point).
- *Fiber Optic Gyroscopes* (FOG): they are similar to the ROGs, except that a fiber optic is used in place of the gas cavity. Thanks to such replacement, the sensor structure is simplified (no gas or mirrors are necessary) and the manufacturing costs are greatly reduced (no precise mirror alignment is required). The scale factor of the sensor is usually enhanced by arranging the fiber optic as a coil with many turns: in practice, the longer the fiber optic is for a given enclosed area, the larger the sensor scale factor is. A weak point of FOGs is their sensitivity to the strain distribution in the optical fiber, induced by temperature changes and accelerations; minimizing such effects is a major concern in FOGs design.

A comprehensive review of many conventional designs and technologies for gyroscopes can be found in (Lawrence, A., 1993; R.R.Ragan (ed), 1984).

2.2 Micromachined gyroscopes

Traditional designs conceived for macro-scale sensors are usually difficult to reproduce in miniaturized devices because of the limitations imposed by the conventional micro-fabrication techniques. For examples, bearings required to mitigate friction and wear of rotating parts, such as spinning wheels or disks, are difficult to manufacture at the micro-scale; alternative designs for frictionless supports based on levitation of any sort (e.g. mechanical, electrostatic/magnetostatic or based on fluid flotation) are failure-prone and not robust enough for commercial applications. Furthermore, because precision in conventional mechanical gyroscopes is related to the angular momentum impressed to the spinning wheel, which in turns is proportional to the mass and the spin rate, it follows that conventional designs become ineffective when dimensions scale down.

Instead of attempting to replicate existing macro-scale designs at the micro-scale level, miniaturized gyroscopes are more conveniently designed by pursuing a completely different working principle, which is better suited for taking advantage of the miniaturization process. In almost all MEMS gyroscopes, the sensor angular velocity is inferred by detecting, on the sensor frame, the motion deflections experienced by a vibrating member. The deflections can be explained by the onset of an apparent force, called *Coriolis force*, which is observed whenever the observer reference frame rotates with respect to a moving body (vibrating

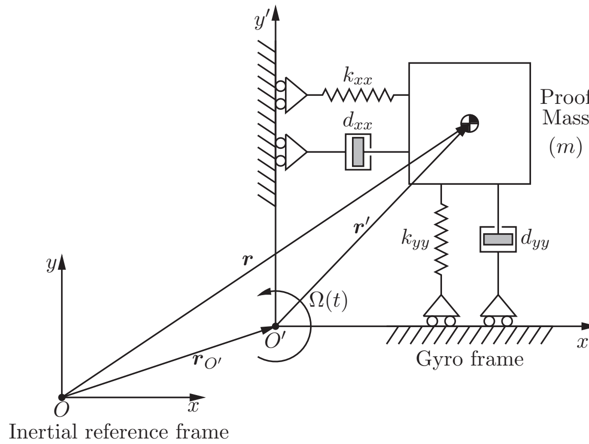

Fig. 1. Simplified lumped-element model of a single axis gyroscope. The gyro frame rotates at an angular rate $\Omega(t)$ about an axis (z'-axis) orthogonal to the $x'O'y'$ plane.

member). A gyroscope adopting this working principle is called *Coriolis Vibrating Gyroscope* (CVG).

The working principle of a CVG can be better understood with the aid of the simplified lumped-element model of a single-axis gyroscope (z-axis gyro) depicted in Fig. 1.

It consists of a proof mass attached to the sensor frame by means of elastic suspensions, in such a way that it can vibrates on the $x'O'y'$ plane with no constraints. The structure has two (ideally orthogonal) modes of vibrations, that are dynamically coupled through the Coriolis force when observed on a sensor-fixed reference frame. In fact, by denoting with $\boldsymbol{r}$ and $\boldsymbol{r}'$ the positions of the proof mass in, respectively, an inertial reference frame and the sensor reference frame, and with $\boldsymbol{r}_{O'}$ and $\boldsymbol{\Omega}$ the position and angular velocity vectors of the sensor frame with respect to the inertial frame, it follows that (Meirovitch, 1970):

$$\dot{\boldsymbol{r}} = \dot{\boldsymbol{r}}_{O'} + \dot{\boldsymbol{r}}' + \boldsymbol{\Omega} \times \boldsymbol{r}' \tag{1}$$

$$\ddot{\boldsymbol{r}} = \ddot{\boldsymbol{r}}_{O'} + \ddot{\boldsymbol{r}}' + 2\,\boldsymbol{\Omega} \times \dot{\boldsymbol{r}}' + \dot{\boldsymbol{\Omega}} \times \boldsymbol{r}' + \boldsymbol{\Omega} \times (\boldsymbol{\Omega} \times \boldsymbol{r}') \tag{2}$$

Regarding accelerations, $\ddot{\boldsymbol{r}}$ denotes the acceleration of the proof mass relative to the inertial frame, $\ddot{\boldsymbol{r}}_{O'}$ is the acceleration of the origin of the sensor frame and $\ddot{\boldsymbol{r}}'$ is the acceleration of the proof mass as measured in the sensor frame. Rewriting the last equation in terms of $\ddot{\boldsymbol{r}}'$ yields:

$$\ddot{\boldsymbol{r}}' = \ddot{\boldsymbol{r}} - \ddot{\boldsymbol{r}}_{O'} - 2\,\boldsymbol{\Omega} \times \dot{\boldsymbol{r}}' - \dot{\boldsymbol{\Omega}} \times \boldsymbol{r}' - \boldsymbol{\Omega} \times (\boldsymbol{\Omega} \times \boldsymbol{r}') \tag{3}$$

The contribution $-\dot{\boldsymbol{\Omega}} \times \boldsymbol{r}'$ to the total acceleration in the sensor frame is known as the *Coriolis acceleration*, while $-\boldsymbol{\Omega} \times (\boldsymbol{\Omega} \times \boldsymbol{r}')$ is the centrifugal acceleration; the remaining term $-\dot{\boldsymbol{\Omega}} \times \boldsymbol{r}'$ is due to a non-constant rotation rate of the sensor frame. With the knowledge of the acceleration $\ddot{\boldsymbol{r}}'$, it is possible to derive the following equations of motion for the proof mass in the sensor reference frame:

$$\boldsymbol{M}\,\ddot{\boldsymbol{r}}' + \boldsymbol{D}\,\dot{\boldsymbol{r}}' + \boldsymbol{K}\,\boldsymbol{r}' = \boldsymbol{F} - \boldsymbol{M}\left[\ddot{\boldsymbol{r}}_{O'} + 2\,\boldsymbol{\Omega} \times \dot{\boldsymbol{r}}' + \dot{\boldsymbol{\Omega}} \times \boldsymbol{r}' + \boldsymbol{\Omega} \times (\boldsymbol{\Omega} \times \boldsymbol{r}')\right] \tag{4}$$

The 3×3 positive definite matrices $\boldsymbol{M}$, $\boldsymbol{D}$ and $\boldsymbol{K}$ are the mass, damping and stiffness matrices; $\boldsymbol{F} = \boldsymbol{M}\ddot{\boldsymbol{r}}$ is the total external force (measured in the inertial frame) applied to the proof mass.
In order to measure the component of the angular velocity around the z'-axis of the sensor reference frame, the proof mass motion can be constrained to lie on the x'-y' plane, by making the spring suspensions along the z'-axis much stiffer than those along the x' and y' directions. Under this assumption, the decomposition of the equations of motion along the two principal directions of vibration yields:

$$m_x\ddot{x}' + d_{xx}\dot{x}' + \left[k_{xx} - m_x(\Omega_y^2 + \Omega_z^2)\right] x' + m_x\left(\Omega_x\Omega_y - \dot{\Omega}_z\right) y' = F_x - m_x\ddot{x}_{O'} + 2m_x\Omega_z\dot{y}' \quad (5)$$

$$m_y\ddot{y}' + d_{yy}\dot{y}' + m_y\left(\Omega_x\Omega_y + \dot{\Omega}_z\right) x' + \left[k_{yy} - m_x(\Omega_x^2 + \Omega_z^2)\right] y' = F_y - m_y\ddot{y}_{O'} - 2m_y\Omega_z\dot{x}' \quad (6)$$

where it has been assumed that the two principal directions of vibrations are aligned with the sensor frame axes, i.e. the $\boldsymbol{D}$ and $\boldsymbol{K}$ matrices are diagonal. With a relatively small sensor bandwidth, i.e. for constant or small varying angular rate inputs, the angular acceleration $\dot{\Omega}_z$ is negligible; moreover, if the angular rate is much smaller than the frequency of the proof mass vibrating motion, then Ω_x^2, Ω_y^2 and $\Omega_x\Omega_y$ can also be neglected. The effect of the linear accelerations $\ddot{x}_{O'}$ and $\ddot{y}_{O'}$ can be compensated either by applying some counterbalancing actuation forces or by adjusting the induced slow trends in the sensor output response, and therefore they can be dropped in the subsequent analysis. Under these circumstances, the equations of motion become:

$$m_x\,\ddot{x}' + d_{xx}\,\dot{x}' + k_{xx}\,x' = F_x + 2m_x\,\Omega_z\,\dot{y}' \quad (7)$$

$$m_y\,\ddot{y}' + d_{yy}\,\dot{y}' + k_{yy}\,y' = F_y - 2m_y\,\Omega_z\,\dot{x}' \quad (8)$$

The conventional mode of operation of a vibration gyroscope consists of driving one mode of vibration (*drive* or *primary mode*) into a controlled-amplitude harmonic oscillation; for an underdamped mode (typical situation in micro-gyroscopes), the oscillation is driven at the vibration mode resonance, in order to take advantage of the mechanical amplification. The remaining modes of vibration (*sense*, *pickoff* or *secondary modes*) are used to sense the angular rate, by measuring the proof mass displacement induced by the Coriolis force. Assuming that the drive and sense modes are directed, respectively, along the x and y axes, the equations of motion for the conventional mode of operation can be written as follows:

$$x' = -X_0 \sin\omega_x t \quad (9)$$

$$\ddot{y}' + \frac{\omega_y}{Q_y}\,\dot{y}' + \omega_{yy}^2\,y' = u_y + 2\,\Omega_z\,\omega_x X_0 \cos\omega_x t \quad (10)$$

where $\omega_x = \sqrt{k_{xx}/m_x}$ and $\omega_y = \sqrt{k_{yy}/m_y}$a are the natural frequencies of, respectively, the drive and sense modes, $Q_y = m_y\omega_y/d_{yy}$ is the quality factor of the second order (under)damped oscillator representing the sense mode dynamics and $u_y = F_y/m_y$ is an external acceleration.
Assuming a cosinusoidal angular rate input $\Omega_z(t) = \Omega\cos\omega_\Omega t$ and no external excitation, i.e. $u_y = 0$, the proof mass displacement produced by the Coriolis acceleration along the sense mode direction is equal to:

$$y(t) := \omega_x X_0\,H_{\Omega+}\,\Omega\cos((\omega_x + \omega_\Omega)t + \phi_{\Omega+}) + \omega_x X_0\,H_{\Omega-}\,\Omega\cos((\omega_x - \omega_\Omega)t + \phi_{\Omega-}) \quad (11)$$

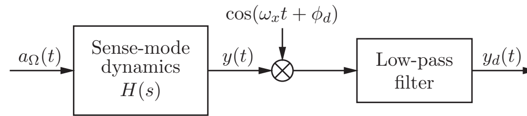

Fig. 2. Synchronous amplitude demodulation scheme used to retrieve the angular rate measurement $\Omega(t)$ from the proof mass displacement $y(t)$. In the block diagram, a_Ω denotes the Coriolis acceleration $a_\Omega = 2\Omega_z \omega_x X_0 \cos \omega_x t$.

where:

$$H_{\Omega\pm} := |H(s)|_{s=j(\omega_x \pm \omega_\Omega)} \qquad \phi_{\Omega\pm} := \angle H(s)|_{s=j(\omega_x \pm \omega_\Omega)} \tag{12}$$

and $H(s)$ is the transfer function of the sense-mode dynamics:

$$H(s) = \frac{1}{s^2 + \frac{\omega_y}{Q_y} s + \omega_y^2} \tag{13}$$

The displacement signal is dual-side-band (DSB) modulated signal, with carrier frequency ω_x: hence, an amplitude demodulation scheme (Fig. 2) can be used to retrieve the information about the modulating signal $\Omega_z(t)$. In fact, by using a demodulating carrier equal to $\cos(\omega_x t + \phi_d)$, the output y_d of the demodulator is equal to:

$$\begin{aligned} y_d(t) &= \text{LPF}[y(t)\cos(\omega_x t + \phi_d)] \\ &= \frac{1}{2}\omega_x X_0 H_{\Omega+} \Omega \cos(\omega_\Omega t + \phi_{\Omega+} - \phi_d) + \frac{1}{2}\omega_x X_0 H_{\Omega-} \Omega \cos(-\omega_\Omega t + \phi_{\Omega-} - \phi_d) \end{aligned} \tag{14}$$

where LPF denotes an ideal (brick-wall) low-pass filtering with corner frequency $\omega_{LPF} \ll \omega_x$ (it is understood that the drive-mode vibration frequency ω_x is designed to be much larger than the sensor bandwidth, i.e. $\omega_{\Omega,\text{MAX}} \ll \omega_x$). For a small sensor bandwidth, it can be assumed that $\omega_x \pm \omega_\Omega \approx \omega_x$, so that:

$$H_{\Omega\pm} \approx H_0 := |H(j\omega_x)| = \frac{1}{\sqrt{(\omega_y^2 - \omega_x^2)^2 + \left(\frac{\omega_x \omega_y}{Q_y}\right)^2}} \qquad \phi_{\Omega\pm} \approx \phi_0 := \angle H(j\omega_x)$$

and:

$$y_d(t) = \omega_x X_0 H_0 \, \Omega \, \cos(\Delta\phi) \cos(\omega_\Omega t) \tag{15}$$

with $\Delta\phi = \phi_{\Omega\pm} - \phi_d = \phi_0 - \phi_d$. Therefore, the demodulator output y_d is proportional to the angular rate input $\Omega_z(t)$. From the last equation it can be noted that the sensor scale factor (see also Sec. 4) depends on the amplitude X_0 of the drive motion, the drive and sense modes natural frequencies ω_x and ω_y, and the sense-mode quality factor (through H_0). In general, sensitivity can be enhanced by increasing the drive mode amplitude X_0 and by lowering the natural frequencies ω_x and ω_y, namely by employing a bulkier proof mass or by softening the elastic suspensions. For a given drive-mode natural frequency ω_x, the sensitivity is maximized when $\omega_y = \omega_x$, i.e. when the two modes are exactly matched (*mode-matching condition*).

3. MEMS gyroscopes technology

3.1 Mechanical structures

As pointed out in Sec. 2, almost all MEMS gyroscopes operate as Coriolis Vibrating Gyroscopes (CVGs). A CVG comprises a mechanical structure with at least two modes of vibration that are dynamically coupled via the Coriolis force, i.e. an apparent force that arises from the relative motion of the vibrating structure and the sensor frame. The normal operation of a CVG consists of exciting one mode of vibration (*driving mode*) at a prescribed amplitude, and detecting the vibrations induced by the Coriolis force on the remaining modes (*sense* of *pickoff* modes).

Several mechanical designs for micromachined CVGs have been either proposed in technical literature or exploited in commercial products. A classification of the main designs is reported below:

- *vibrating beams*: they consists of tiny clamped-free beams (*cantilevers*) or clamped-clamped beams (*bridges*) that are driven into flexural vibration on a plane. Then, in response to a rotation, the beam starts vibrating along an orthogonal direction, and this motion can be used to infer about the angular rate input - see Fig. 3.

  Several designs involving beam structures have been proposed in literature, especially in connection with the usage of piezoelectric materials (Soderkvist, 1991). A vibrating beam structure has also been chosen for the development of the first silicon integrated micromachined CVG back in 1981 (O'Connor & Shupe, 1983).

  An example of a vibrating beam gyroscope consisting of a silicon-based microcantilever fabricated with bulk-micromachining techniques is reported in (Maenaka et al., 1996). Beam actuation is provided by a piezoelectric element; the Coriolis-induced vibration is electrostatically detected by measuring the capacitance changes between the beam and dedicated sensing electrodes. A combined beam-mass structure with a composite beam is proposed in (Li et al., 1999). The two-section composite beam structure is designed to have a vertical and a lateral highly compliant vibrating modes. The vertical mode is excited by

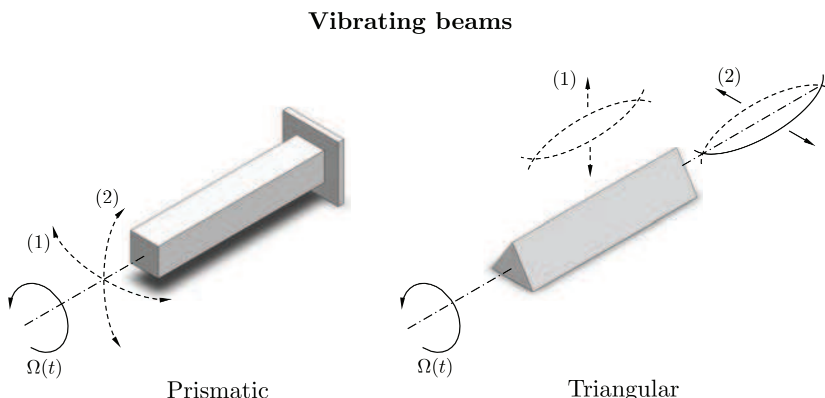

Fig. 3. Most conventional types of vibrating beam CVGs. In figure, $\Omega(t)$ is the input angular rate, (1) is the primary vibration mode, and (2) is the vibration response due to Coriolis forcing.

means of electrostatic actuation, while the Coriolis-induced vibration on the lateral mode is detected by means of embedded piezoresistors.

A commercial product featuring a vibrating beam design is the *Gyrostar*, a piezoelectric CVG produced by (muRata, 2003). It consists of an equilateral prism which is excited into flexural vibration by using piezoelectric elements applied to its sides. The beam is attached to the supporting frame at positions along the beam length that correspond to node points for the free-free flexural modes of vibration: this choice ideally decouples the beam from the supporting structure. The vibrations induced by the Coriolis force on the secondary mode are detected again by using piezoelectric transducers.

A structure resembling a vibrating beam gyroscope can also be found in nature: the *halteres*, a pair of vibrating knob sticks found in many two-winged insects, are indeed a pair of tiny vibrating beam CVGs that are used to stabilize and control the flight attitude (Nalbach, 1993; Nalbach & Hengstenberg, 1994).

- *vibrating forks*: they contain a pair of proof masses that are oscillated with the same amplitude, but in opposite directions. In a traditional fork structure, the tines are excited to resonate in anti-phase in the plane of the fork (drive mode); then, when the sensor rotates, the tines start oscillating along the perpendicular direction to the plane, thus generating a torque that excites the torsional mode around the stem. Forks can be of *single*, *dual* or *multi-tines* types; the latter type is used in order to increase sensitivity and reject common-mode errors (caused by geometrical asymmetries).

  Most of the Quartz Rate Sensors (QRS) that populated the market before the advent of silicon micromachined gyroscopes had a vibrating forks structure. For example, the first

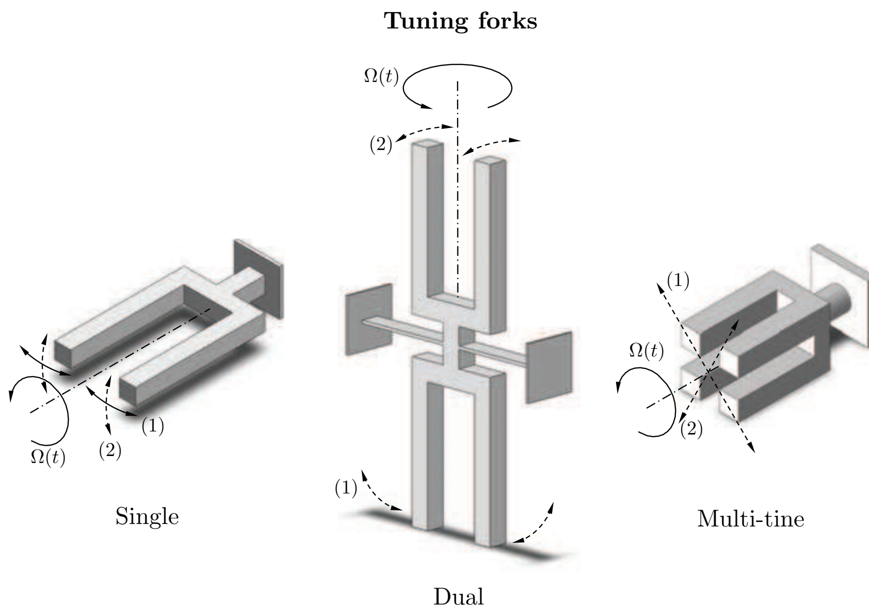

Fig. 4. Most conventional types of tuning fork CVGs. In figure, $\Omega(t)$ is the input angular rate, (1) is the primary vibration mode, and (2) is the vibration response due to Coriolis forcing.

miniaturized gyroscope to have been introduced in the market back in 1980, namely the Systron Donner/BEI QRS, was a H-shaped two-sided tuning fork gyroscope (Madni et al., 2003) (see Fig. 10-a). Epson-Toyocom is another company selling QRS whose structure is a double-T tuning fork with external vibrating tines and central stationary sensing arm.

In silicon micromachined vibrating forks gyroscopes, the fork tines are usually replaced by anti-phase resonating seismic masses vibrating on a common plane (Bernstein et al., 1993). The plane can be either parallel to the substrate, such as in Bosch SMG074 (Lutz et al., 1997), Analog Devices ADXRS150 (Geen et al., 2002) and STMicroelectronics LISY300AL (Oboe et al., 2005), or normal to the substrate, such as in the Invensense IDG family (Nasiri & Flannery Jr., 2007) (see Fig. 9).

A silicon micromachined gyroscope with a conventional vibrating fork structure (i.e. a structure comprising a fork with vibrating tines) is the angular-rate sensor produced by Daimler-Benz (Voss et al., 1997).

- *vibrating plates*: they have a resonant element consisting of a tiny plate, attached to the sensor outer frame by means of linear or torsional elastic suspensions (Tang et al., 1989). Forced vibrations can be induced either along a straight line (*linear plate* configuration (Clark et al., 1996; Tanaka et al., 1995)) or around an axis of rotation (*angular disk* configuration (Geiger et al., 1998; Juneau et al., 1997; Rajendran & Liew, 2004)). Melexis MLX90609-N2 is an example of a commercial MEMS gyroscope based on a vibrating plate structure (actually, a single gimbaled mass with translation drive).The vibrating angular disk structure is exploited in many commercial dual-axis pitch and roll MEMS gyroscopes: examples include the Bosch SMG060 and the STMicroelectronics LPR family.

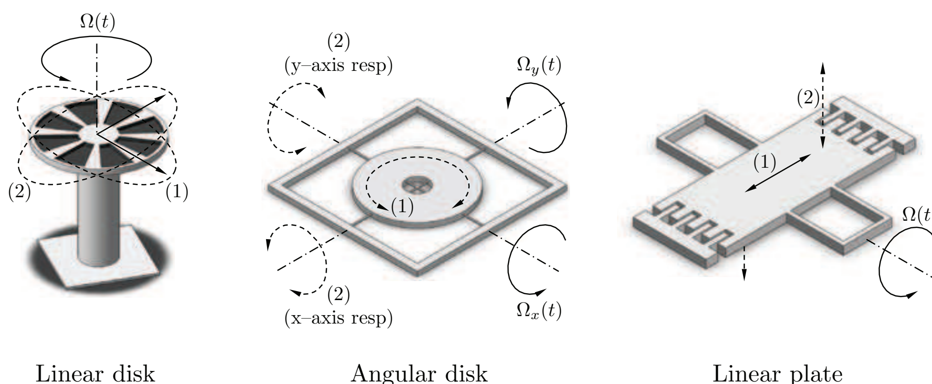

Fig. 5. Most conventional types of vibrating plate CVGs. In figure, $\Omega(t)$, $\Omega_x(t)$ and $\Omega_y(t)$ are the input angular rates, (1) is the primary vibration mode, and (2) is the vibration response due to Coriolis forcing.

- *vibrating shells*: they have circular shapes, such as *rings*, *cylinders* or *hemispheres*, which are set into a standing-wave vibration through external forcing. Whenever the sensor undergoes a rotation around its axis of symmetry, the vibration pattern, consisting of nodes and antinodes of the forced standing-wave, moves with respect to the external case; its

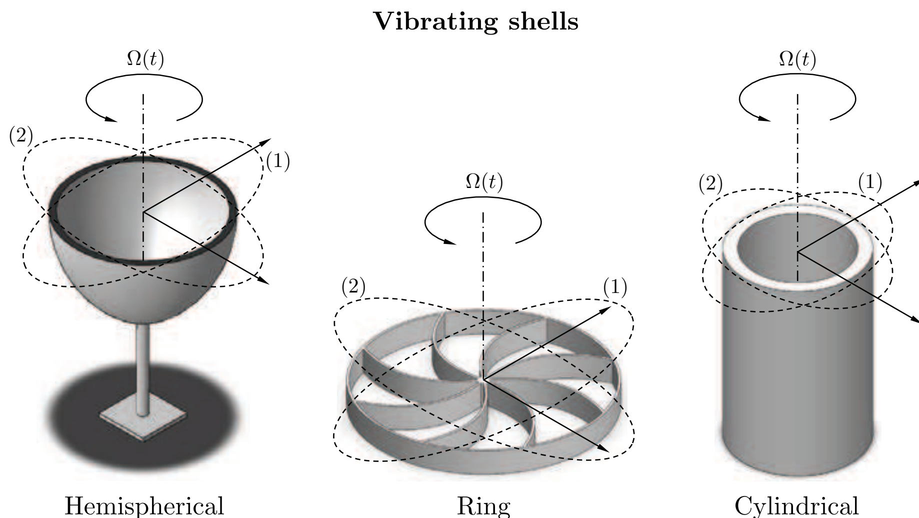

Fig. 6. Most conventional types of vibrating shell CVGs. In figure, $\Omega(t)$ is the input angular rate, (1) is the initial vibration pattern and (2) is the pattern after rotation.

motion can be detected by dedicated displacement sensors and used to infer about the angular rate input.

Most of the MEMS gyroscopes produced by Silicon Sensing Systems (SSS) are based on a vibrating ring structure (Fell, 2006; Hopkin et al., 1999). Delphi Delco Electronics has also reported in (Chang et al., 1998) the design of a vibrating ring gyroscope manufactured by electroplating on a fully processed CMOS wafer.

A vibrating cylinder structure can be found in NEC-Tokin ceramic gyroscopes; the structure actually consists of a cylindrical piezoelectric ceramic oscillator with embedded electrodes for electrostatic detection of Coriolis-induced vibrations (Abe et al., 1992).

Vibrating hemispherical shells have been traditionally used in macro-sized gyroscopes, such as the Delco Hemisperical Resonator Gyro (HRG) (Lawrence, A., 1993). The device consists of a hemispherical shell made of fused silica, which is encased within a sealed vacuum housing. A standing-wave vibration is electrostatically induced on the shell metal-coated rim; wave pattern shifts caused by sensor rotations are detected with capacitive pick-offs. Recently, a micromachined gyroscope with a similar structure has been patented (Stewart, 2009).

- gyroscopes based on the *surface acoustic wave (SAW)* technology.

  In a SAW gyroscope, a set of metallic electrodes (interdigital transducer - IDT) patterned on the surface of a piezoelectric substrate is used to generate a Rayleigh standing-wave. A Rayleigh wave is a mechanical transverse wave whose shear component is normal to the substrate surface, and whose energy is concentrated within one wavelength of the substrate surface (Drafts, 2001; Vellekoop, 1998). The out-of-plane vibration of the particles near the surface is perturbed by the Coriolis force whenever the piezoelectric substrate undergoes a rotation (about an axis vertical to its surface). Such perturbation produces a secondary standing wave polarized parallel to the substrate surface, whose amplitude is

proportional to the sensor angular rate: hence, by sensing the amplitude of the secondary wave with an additional IDT, it is possible to retrieve a measurement of the input angular rate.

Some design examples of SAW MEMS gyroscopes are presented in (Jose et al., 2002; Kurosawa et al., 1998; Liu & Wu, 2007).

There have been very few attempts to depart from the conventional designs based on the CVG working principle; the most noticeable examples are:

- gyroscopes based on the conservation of the angular momentum in levitated spinning disks, similarly to conventional (macro-sized) mechanical flywheel gyroscopes. Both the electrostatic (Damrongsak & Kraft, 2005; Ellis & Wilamowski, 2008) and magnetic levitation principles (Dauwalter & Ha, 2005; Shearwood et al., 2000) have been exploited.
- thermal convective gyroscopes.Their working principle is based on the detection of convective heat flow deflections induced by the Coriolis acceleration. The sensor proposed in (Zhu et al., 2006) consists of a hermetically sealed gas chamber obtained by etching a small cavity on a silicon substrate. The cavity contains a suspended central heater that is used to induce a regular gas flow within the chamber, and four suspended thermistor wires placed symmetrically on both sides of the heater for measuring local changes in the gas flow. By measuring the voltage imbalances among the four thermistors readouts (using a Wheastone bridge circuit) it is possible to estimate both angular velocities and linear accelerations.
- gyroscopes using liquid or gas jet flows. In the prototype reported in (Yokota et al., 2008), a jet flow in an electro-conjugate fluid (ECF) is generated by imposing an electric field between two brass electrodes dipped in the liquid. When the sensor is rotated, the jet flow is deflected by the Coriolis acceleration. The deflection, which is an indirect measure of the input angular rate, is sensed as an unbalancing in the electrical resistance of two tungsten hot-wires placed on the sidewalls of the fluid channel.

  A similar design is proposed in (Zhou et al., 2005), except that a gas is used instead of an ECF.
- Micro-Opto-Electro-Mechanical (MOEMS) gyroscopes. This technology is still under development, and no accurate MOEMS gyroscopes exist yet. The goal is the development of a miniaturized optical device that, similarly to a standard interferometric optical gyroscope, relies on the Sagnac effect for measuring a rotation rate. The main design issue for micro-optical gyroscopes is how to create optical path lengths that are large enough to sense useful angular velocities (i.e. greater in strength than the noise inherent in the measurement). In the AFIT MiG prototype reported in (Stringer, 2000), the elongation of the optical path is achieved by creating a spiral path with a set of suitably arranged micro-mirrors placed above the silicon die.

3.2 Fabrication technologies

There are fundamentally two alternative technologies available for the fabrication of micromechanical devices: *bulk micro-machining* and *surface micro-machining* techniques.

- In *bulk micro-machining* (Kovacs et al., 1998) the microstructures are formed by selectively removing (*etching*) parts from a bulk material, which is typically a silicon crystal. The etching process can be performed by either dipping the silicon wafer into an etching solution (*wet etching*) or by exposing the material to vapors or glow-discharge plasmas

of chemically reactive gases (*dry etching*). Protective masks are applied on the surface of the bulk material in order to avoid the exposure to etchants: thus, etching takes place only on those portions that are not covered by a layer of protective material. Most wet etching is *isotropic*, meaning that the etching rate does not depend on the orientation of the substrate; nevertheless, for particular etchants, *anisotropic* (i.e. orientation-dependent) wet etching can occur, so that the etching rate along the direction of a certain crystal axis can be hundreds of times greater than others. Larger levels of directionality can be achieved with anisotropic dry etching techniques, such as DRIE (*Deep Reactive Ion Etching*), in which the direction perpendicular to the exposed surface is etched much faster than the direction parallel to the surface. The depth of the etched features can be controlled by either controlling the exposure time to etchants (once the etching rate is known) or by using some kind of etch-stopping technique or material.

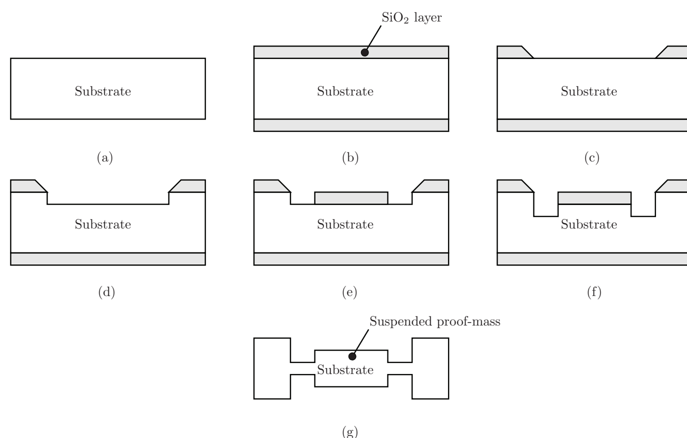

Fig. 7. Typical steps in a bulk micromachining process: (a) substrate preparation - typically, a $500 \div 700\,\mu m$ thick single silicon (Si) crystal; (b) deposition of a silicon dioxide (SiO_2) layer - typical thickness: $1 \div 2\,\mu m$; (c) patterning (photoresist deposition + optical lithography) and etching of the SiO_2 layer; (d) substrate etching; (e) deposition of SiO_2 layer for a selective area (repetition of step (b)); (f) substrate etching for creating deeper trenches (repetition of step (f)); (g) creation of a suspended structure (e.g. a proof mass) after repeating steps (a) $\div$ (f) on the bottom side of the substrate and removing the residual SiO_2 at both sides.

- In *surface micro-machining* (Bustillo et al., 1998; Howe et al., 1996), the microstructures are formed by by depositing, growing and etching different structural layers on top of a substrate. Since the substrate acts only as a supporting structure, it can be made of inexpensive materials such as plastic, glass, quartz, ceramic or other piezoelectric materials (Kotru et al., 2008), instead of the more expensive single-crystal silicon used for IC (integrated circuits) fabrication. On top of the substrate, several layers can be deposited, patterned and released; surface *planarization* is usually required before the deposition of every structural layer, in order to prevent critical issues during photolithography, such as the limited focus depth of high-resolution lithographic tools over non-planar surfaces, and etching - anisotropic etching of non-planar surfaces may leave behind several stringers of unetched material. Apart of structural layers, the fabrication of complex structure with

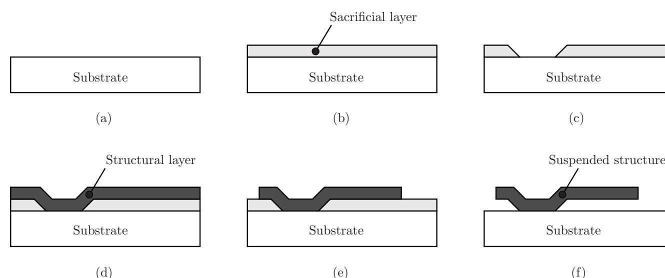

Fig. 8. Typical steps in a surface micromachining process: (a) substrate preparation - typically, a $500 \div 700\,\mu m$ thick single silicon (Si) crystal; (b) deposition of a sacrificial layer - typically, a $1 \div 2\,\mu m$ thick silicon dioxide (SiO_2) layer; (c) creation of a hole by patterning (photoresist deposition + optical lithography) and etching of the sacrificial layer; (d) deposition of a structural layer - typically, a $1 \div 5\,\mu m$ thick polysilicon layer; (e) shape definition by patterning and etching of the structural layer; (f) release of the suspended structure (e.g. a cantilever beam).

suspended or freely moving parts may require the deposition of so-called *sacrificial layers*, i.e. layers that are selectively removed (*release etch* step) after growing one or more thin-film structures above them. Thin-film deposition can be realized with several techniques, such as physical or chemical vapor deposition (PVD or CVD, respectively), electrodeposition, spin coating and Sol-Gel deposition. Thicker structures can be created by either using epi-poly as structural material, or by bonding together two or more silicon wafers, using wafer bonding techniques such as silicon-to-silicon bonding, silicon-on-insulator (SOI) bonding, anodic bonding, adhesive bonding, etc.

3.3 Actuation and sensing mechanisms

Several methods have been exploited so far for generating and detecting vibrating motions inside CVGs. Nevertheless, the foremost methods in industry practice are based on electrostatic and piezoelectric principles, mainly because of the easiness of fabrication, miniaturization and integration with standard manufacturing processes of the IC industry.

In electrostatic actuation, the attractive (repulsive) forces arising on oppositely (similarly) electrically charged objects are used to generate motion; conversely, the capacitance change experienced by electrically charged objects moving apart each other is exploited to detect motion. Typically, an electrostatic actuator or sensor resembles a capacitor with moving plates: indeed, this is the case for the *parallel-plate* and *comb-fingers* structures (Boser, 1997; Senturia, 2001). An example of a MEMS gyroscope exploiting electrostatic actuation and sensing is reported in Fig. 9.

In piezoelectric actuation, the property (*inverse piezoelectric effect*) of certain materials (e.g. quartz, ceramics, special alloys or piezoelectric polymers) to change their shape when subjected to an electric field is effectively exploited to generate a mechanical deformation or displacement. With regards to sensing, either the *direct piezoelectric effect* (Kotru et al., 2008; Soderkvist, 1991) (generation of an electric field in response to a mechanical strain) or the *piezoresistive effect* (Li et al., 1999; Voss et al., 1997) (change of electrical resistance in response to a mechanical stress) are effectively used to sense the Coriolis-induced motion.

Except for electrostatic and piezoelectric methods, rather few alternatives have been investigated and tested; examples of typical solutions presented in literature include designs based on thermal (Shakoor et al., 2009) and magnetic (Paoletti et al., 1996; Tsai et al., 2009) actuation, or optical sensing (Bochobza-Degani et al., 2000; Norgia & Donati, 2001).

3.4 Onboard electronics

The onboard electronics is necessary for:

- *driving and sustaining the oscillations of the vibrating member*. Two requirements must be fulfilled when generating the driving motion: first, the oscillation amplitude must be controlled with a high level of accuracy, since the stability of the sensor scale factor depends on it (see Eqn. 15); second, the oscillation frequency should be as close as possible to the resonant frequency of the vibrating member, in order to maximize the efficiency in motion generation. These two requirements are usually accomplished by employing a dedicated feedback control loop (*driving loop*), which basically excites the vibrating member with a properly gain and phase adjusted version of the driving mode detected motion. The phase is adjusted to meet the *Barkhausen's condition*, thus actually implementing an electromechanical (sinusoidal) oscillator (i.e. an electronic oscillator with a mechanical resonating element); the gain is adjusted to regulate the oscillation amplitude to the desired set-point. Details about the working principle and implementation of a driving loop can be found in (M'Closkey & Vakakis, 1999; Oboe et al., 2005) (conventional design) and (Dong & Avanesian, 2009; Leland et al., 2003) (unconventional designs based on adaptive control schemes).

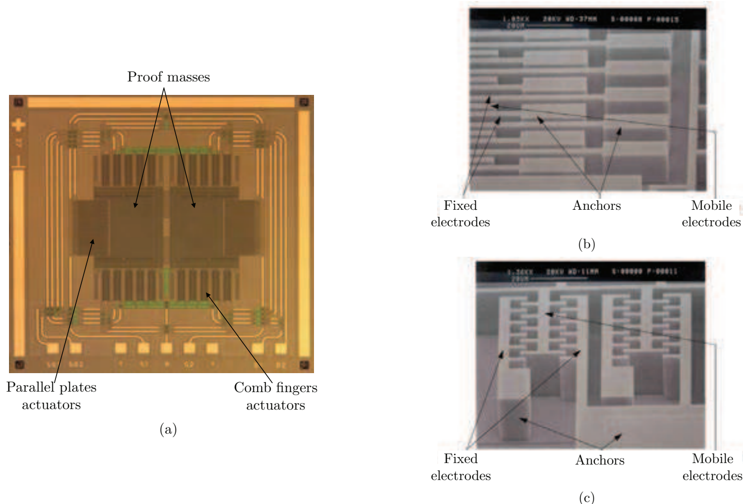

Fig. 9. Example of electrostatic actuation and sensing in a MEMS gyroscope: (a) ST Microelectronics LISY300AL single-axis yaw-gyroscope (die photo); (b) parallel-plate electrodes used for sensing the Coriolis-induced vibration along the sense axis; (c) comb-fingers structures used for actuating/sensing the proof-mass motion along the drive axis.

- *retrieving an angular velocity measurement from the sensing mode vibration*. Several stages are usually involved in retrieving a reliable measure: first, the Coriolis-induced motion must be transduced into an electric signal, possibly ensuring a sufficiently high signal-to-noise ratio. Second, the transduced signal must be demodulated with a carrier that is synchronized with the driving motion, in order to obtain a baseband signal which is proportional to the angular velocity; and finally, the demodulated signal must be conditioned (e.g. scaled, filtered, digitized, etc.).
- *reducing the interaction between the driving and sensing loops*. Differently from the ideal situation described in Sec. 2.2, in the real situation there is always a spurious motion along the sense axis that is directly proportional to the drive vibration. This motion, called *quadrature error*, is mainly due to a lack of orthogonality between the drive and sense axes, which in turn results from structural asymmetries due to fabrication defects and imperfections. The quadrature error requires to be compensated, since it detrimentally affects the measurement. Usual compensation methods consists of either rebalancing the mechanical structure (with mechanical or electrostatic methods - (Painter & Shkel, 2003;

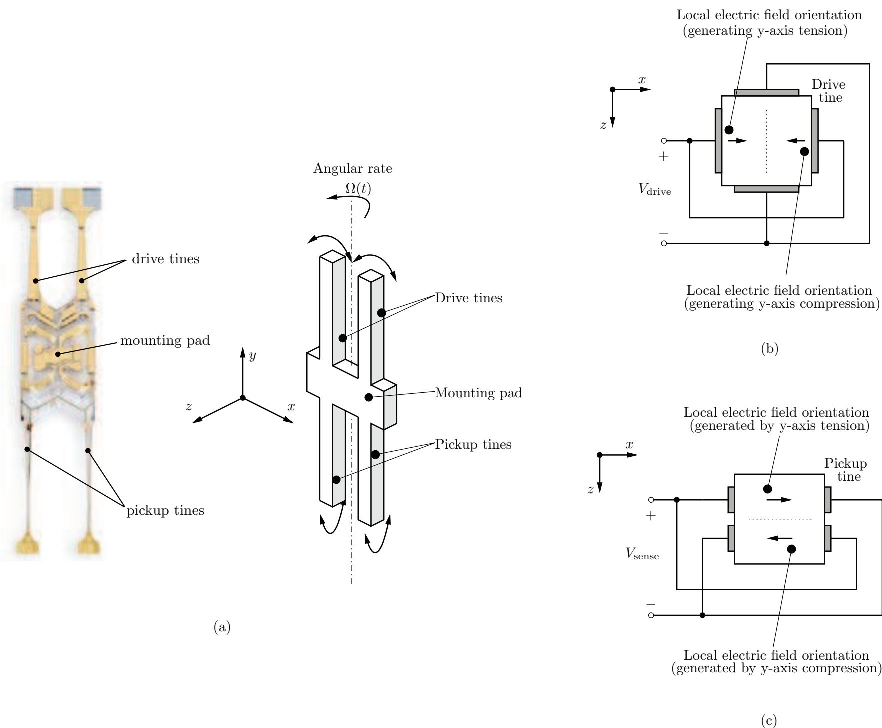

Fig. 10. Example of piezoelectric actuation and sensing in a micro-gyroscope: (a) Systron Donner Quartz Rotation Sensor (QRS) (quartz cut axis orientation ≡ z-axis) (Gupta & Jenson, 1995; Knowles & Moore, 2004); (b) electrodes configuration for generating the drive tine bending vibration; (b) electrodes configuration for sensing the pickup tine bending vibration.

Weinberg & Kourepenis, 2006)) or canceling the error from the measurement (using a feed-forward cancellation scheme - (Antonello et al., 2009; Saukoski et al., 2007)).

- *improving sensor linearity and bandwidth*. This is usually achieved by exploiting a closed-loop sensing interface, in which the sense motion is nulled by employing a control loop. The feedback signal used for nulling the sense motion contains the angular velocity information, which can be extracted with a basic synchronous baseband demodulation circuit. When a digital output must be provided, the feedback signal can be oversampled and quantized with a coarse quantizer: in this case, the closed-loop sensing interface behaves as a (electromechanical) $\Sigma\Delta$ modulator (Dong et al., 2008; Petkov & Boser, 2005).
- *improving scale factor thermal stability*. A temperature compensation loop can be sometimes integrated on-board to reduce the sensitivity of the scale factor to temperature variations (Jiancheng & Jianli, 2009).

Additional electronic functions may include self test and calibration, bias compensation, etc.

4. Industrial requirements

The specifications and test procedures for a single-axis CVG-based angular rate sensor have been standardized in (*IEEE Standard Specification Format Guide and Test Procedure for Coriolis Vibratory Gyros*, 2004). The standard requirements for a CVG are specified in terms of its *performances*, its *mechanical* and *electrical interface* characteristics, the *environmental* conditions, the sensor *life time* and *reliability* (usually measured as *Mean Time Between Failure* - MTBF).
The performance of a CVG is specified according to the following quantities, whose definitions are taken from (*IEEE Standard for Inertial Sensor Terminology*, 2001):

- *Input range*: the interval between the input limits within which a quantity is measured. The *input limits* are defined as the extreme values of the input, generally plus or minus, within which performance is of the specified accuracy. The *full-scale* (FS) input is the maximum magnitude of the two input limits.
- *Accuracy* (or *linearity error*): the deviation of the output from a least-squares linear fit of the input-output data. It is generally expressed as a percentage of the input full-scale, or a percent of output, or both.

  The definition implicitly assumes that the ideal sensor exhibits a *linear* input-output behavior (i.e. the static input-output sensor characteristic is a linear function).
- *Scale factor* [1] : the ratio of a change in output to a change in the input intended to be measured, typically specified in $[V/°/s]$. It is evaluated as the slope of the least squares straight line fit to input-output data.

  In the ideal case, the scale-factor is constant over both the entire input range and the whole sensor lifespan. In the real case, the following quantities are used to judge the scale factor quality:
  - *asymmetry error*: the difference between the scale factor measured with positive input and that measured with negative input, specified as a fraction of the scale factor measured over the input range.

[1] Sometimes the term *sensitivity* is used as a synonym for scale factor. However, according to (*IEEE Standard for Inertial Sensor Terminology*, 2001), the term sensitivity is reserved for denoting the ratio of a change in output to a change in an *undesirable* or *secondary input*.

  - *scale factor stability*: the variation in scale factor over a specified time of continuous operation. Ambient temperature, power supply and additional factors pertinent to the particular application should be specified.
  - *scale factor sensitivities*: the ratio of change in scale factor to a change in an undesirable input, such as the steady state operating temperature (*scale factor temperature sensitivity*) or the constant acceleration along any axis (*scale factor acceleration sensitivity*). Additional sensitivities may be specified such as those due to variations in supply voltage (including frequency, voltage, ripple, starting and operating current), orientation, vibration, magnetic field, radiation, and other environments pertinent to the particular application.

- *Resolution*: the smallest input change, for inputs greater than the noise level, that can be reliably detected. It is usually evaluated as the minimum input change that produces a change in output equal to some specified percentage (at least 50%) of the change in output expected using the nominal scale factor.
- *Drift rate*: the portion of gyro output that is functionally independent of input rotation.
  The systematic component of the drift rate (*systematic drift rate*) includes:
  1. *Bias* (or *zero rate output* - ZRO): the average over a specified time of gyro output measured at specified operating conditions that has no correlation with input rotation. Bias is typically expressed in $[^\circ/s]$ or $[^\circ/hr]$.
  2. *Environmentally sensitive drift rate*: the components of systematic drift rate that are sensitive to temperature (steady state, gradient, ramp), acceleration, vibration and other quantities.

  The random component of the drift rate (*random drift rate*) includes:
  1. *Angle Random Walk* (ARW): the angular error buildup with time that is due to white noise in angular rate, typically expressed in $[^\circ/hr/\sqrt{hr}]$ or $[^\circ/s/\sqrt{hr}]$.
  2. *Rate Random Walk* (RRW): the drift rate error buildup with time that is due to white noise in angular acceleration, typically expressed in $[^\circ/hr/\sqrt{hr}]$.
  3. *Bias Instability*: the random variation in bias as computed over specified finite sample time and averaging time intervals, characterized by a $1/f$ power spectral density, typically expressed in $[^\circ/hr]$.
- *Bandwidth*: the range of frequency of the angular rate input that the gyroscope can detect. Typically specified as the cutoff frequency coinciding to the $-3\,dB$ point. Alternatively, the frequency response or transfer function could be specified.
- *Activation time*: it includes the *turn-on time*, i.e. the time from the initial application of power until a sensor produces a specified useful output, though not necessarily at the accuracy of full specification performance, and the *warm-up time*, i.e. the time from the initial application of power to reach specified performance under specified operating conditions.

The mechanical and electrical requirements are usually specified in terms of:

- *Outline*, *mounting dimensions*, *weight*
- *Gyro axes*: the *input axis* (IA) is the axis about which a rotation of the case causes a maximum output; the *input reference axis* (IRA) is the direction of an axis (ideally parallel to an input axis) as defined by the case mounting surfaces, or external case markings, or both. In case of a multi-axis gyroscope, more than one IA (and, correspondingly, IRA) can be defined.

- *Seal*: CVGs may be sealed using vacuum, gas or ambient environment.
- *Acoustic noise emission*
- *Electrical impedances*: load impedances and impedances of excitation, monitoring, temperature sensing and test circuits.
- *Input power*, *grounding*
- *Output signals*: the type and characteristics of output signals, such as analog voltage or current, parallel or serial digital, or incremental angle pulses.
- *Electromagnetic interference* and *electrostatic discharge* (ESD) *immunity*.

The environmental requirements specify the environmental conditions (limits) and perturbations during storage, transport and/or operation under which the sensor preserves its functionality. Environmental characteristics account for:

- *Linear* and *angular accelerations*: both the acceleration (axis, direction, intensity) and exposure time should be defined.
- *Linear* and *angular vibrations*: both axes and direction of vibration should be defined. For a deterministic vibration, specifications include the type of vibration (e.g. sinusoidal) and its characteristics (e.g. amplitude, frequency sweep range, exposure time). For a random vibration, its spectral characteristic (e.g. power spectral density - PSD) is usually specified.
- *Mechanical shock*: it is specified in terms of axis, direction, wave shape, intensity (usually measured as a peak value in $[m/s^2]$ or a multiple of the gravity acceleration g) and duration.
- *Temperature range*
- *Others*: may include ambient air pressure, humidity, electromagnetic fields, etc.

Conventionally, gyroscopes are classified into three different categories based on their performance: *inertial-grade*, *tactical-grade*, and *rate-grade* devices (Yazdi et al., 1998). Table 1 summarizes the requirements for each of these categories.
RLGs, together with HLGs (R.R.Ragan (ed), 1984), are currently the angular rate sensors with highest performance available in the market, and exhibit inertial grade performances. They are used in the most demanding applications, especially those requiring extremely high scale factor stability (typically, high precision space applications). FOGs normally achieves tactical grade performances, while typical MEMS CVGs seldom exceed the rate grade performance level, which is however satisfactory for most of the automotive and consumer electronics applications.

Parameter	*Rate grade*	*Tactical grade*	*Inertial grade*
Angle Random Walk $[°/\sqrt{hr}]$	> 0.5	$0.5 \div 0.05$	< 0.001
Bias drift $[°/hr]$	$10 \div 1000$	$0.1 \div 10$	< 0.01
Scale factor Accuracy [%]	$0.1 \div 1$	$0.01 \div 0.1$	< 0.001
Full Scale Range $[°/s]$	$50 \div 1000$	> 500	> 400
Max. Shock in 1 ms [gs]	10^3	$10^3 \div 10^4$	10^3
Bandwidth, Hz	> 70	$\simeq 100$	$\simeq 100$

Table 1. Performance requirements for different classes of gyroscopes

5. Benchmark tests for two commercial products

5.1 Invensense IDG-650 Dual-Axis Pitch & Roll MEMS Gyroscope

The Invensense IDG-650 (Invensense, 2010) is a dual-axis MEMS gyroscope consisting of two independent out-of-plane resonating tuning fork CVGs (for pitch and roll axes) integrated on the same silicon die. The MEMS and CMOS integrated circuit (IC) are electrically connected together through wafer level bonding, in such a way that the mechanical structure is covered and hermetically sealed at the wafer level (*Nasiri-Fabrication* - patent protected). The hermetic sealing improves the sensor resistance to humidity, high temperature and electromagnetic/radio frequency interferences (EMI/RFI). The sensor has selectable scale factors and full scale ranges ($FS = \pm 2000^{\circ}/s$ for faster motions, or $FS = \pm 440^{\circ}/s$ for slower motions). Both the output measurements are thermally compensated by an internal compensation circuit, comprising an integrated onboard temperature

5.2 STMicroelectronics LPR530AL Dual-Axis Pitch & Roll MEMS Gyroscope

The STMicroelectronics LPR530AL (STMicroelectronics, 2010) is a dual-axis MEMS gyroscope capable of measuring angular rates along pitch and roll axes. The mechanical sensing element is a vibrating disk fabricated using STMicroelectronic's proprietary surface micromachining process called *ThELMA* (*Thick Epipoly Layer for Microactuators and Accelerometers*). The mechanical element is obtained by etching a thicker polysilicon epitaxial layer ($\approx 15\mu m$) grown on top of a sacrificial oxide layer ($\approx 2\mu m$), which is removed at the end of the process (release step) by isotropic etching. A second wafer is bonded to the substrate with the purpose of creating a protecting case for the micromechanical structure. The ThELMA micromachined mechanical element and the CMOS controller are finally assembled together in the same chip (hybrid solution: two chips in a single package) either in a side-by-side or a stacked configuration.

	STM LPR530AL	IS IDG-500	IS IDG-650	
• *Scale factor*	0.83	2	0.5	$mV/^{\circ}/s$
• *Scale factor* (× 4.5)	3.33	9.1	2.27	$mV/^{\circ}/s$
• *Scale factor calibration tolerance*	5	6	6	%
• *Scale factor calibration drift over specified temperature* ($T_A = 25^{\circ}$)	0.034	0.067	0.067	$\%/^{\circ}C$
• *Full-scale*	1200	500	2000	$^{\circ}/s$
• *Full-scale* (× 4.5)	300	110	440	$^{\circ}/s$
• *ZRO level*	1.23	1.35	1.35	V
• *ZRO tolerance*	80	250	150	mV
• *ZRO temperature sensitivity over specified temperature* ($T_A = 25^{\circ}$ C)	0.083	0.417	0.667	$^{\circ}/s/^{\circ}C$
• *phase delay* at 10 Hz	4.0	4.5	4.5	$^{\circ}$
• *Turn-on time* (typ)	200	50	50	ms
• *Turn-on-time* (max)	200	200	200	ms
• *Total RMS noise*	1.4	0.8	0.3	mV
• *Nonlinearity*	1	1	1	% of FS
• *Cross-axis sensitivity*	1	1	1	% of FS
• *Supply voltage*	$2.7 \div 3.6$	$2.7 \div 3.3$	$2.7 \div 3.3$	V
• *Current absorption*	6.8	7	7	mA
• *Temperature range*	$-40 \div 85$	$-20 \div 85$	$-20 \div 85$	$^{\circ}C$
• *Package size*	$5 \times 5 \times 1.5$	$4 \times 5 \times 1.2$	$4 \times 5 \times 1.2$	mm

Table 2. Specifications comparison for the gyroscopes under test

5.3 Comparative tests

The results of our comparative tests are briefly summarized in the following paragraphs. Parts have been tested on a single-axis precision positioning and rate table (Aerosmith, 2005), providing the desired angular rate profiles. An additional integral thermal chamber has been installed on the table to allow thermal sensitivity/stress analyses.

5.3.1 ZRO temperature sensitivity

The ZRO has been measured by setting the default FS (i.e. full-scale $\times$ 4.5 in Tab. 2) for both STM and IS sensors, and by varying the temperature over the range $-40°\ C \div 85°\ C$ in steps of $5°\ C$. As shown in Fig. 11, the ZRO of the STM sensor appears to be slightly more insensitive to temperature variations than the IS sensor; however, the temperature sensitivities of both sensors are within specifications.

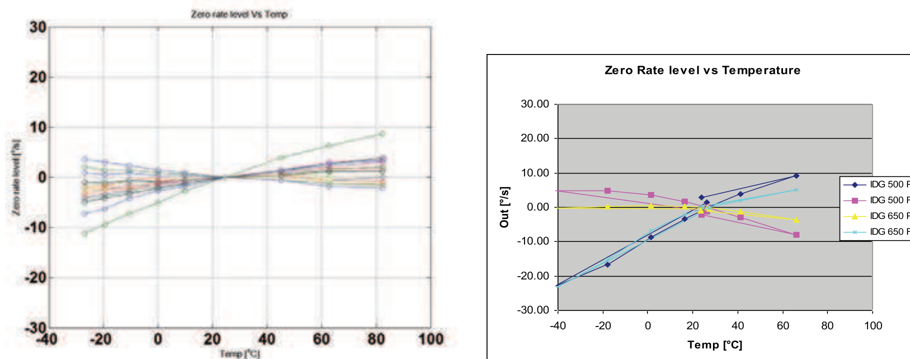

Fig. 11. ZRO temperature sensitivity test results: STM (left); IS (right).

5.3.2 ZRO mechanical stress sensitivity

The ZRO has been measured after applying different calibrated vertical loads on the sensor package, by means of a load cell. It has been noted that only the STM sensor has a ZRO that is immune to the applied mechanical stress; for what concerns the IS sensor, the ZRO variation exceeds the value of $30°/s$ as the vertical load varies over the range $0 \div 4\,kg$ (see Fig. 12).

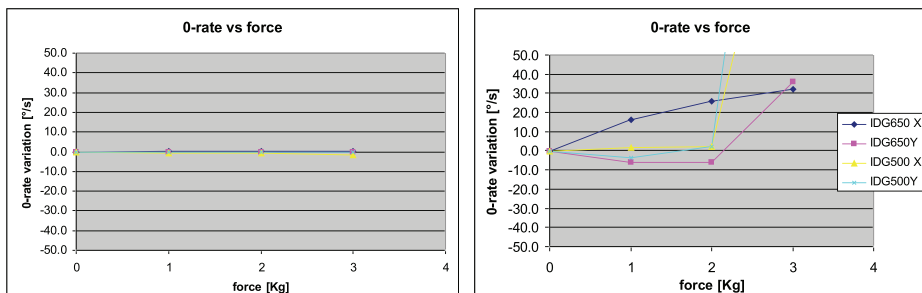

Fig. 12. ZRO mechanical stress sensitivity test results: STM (left), IS (right).

5.3.3 Scale factor temperature sensitivity

Scale factor measurements have been done at a constant angular rate of $150^{\circ}/s$, and by varying the temperature over the range $-40^{\circ}\,C \div 85^{\circ}\,C$ in steps of $5^{\circ}\,C$. On average, both the STM and IS sensors exhibit a scale factor temperature sensitivity below $0.05\,\%/^{\circ}C$ and thus within specifications (see Fig. 13) .

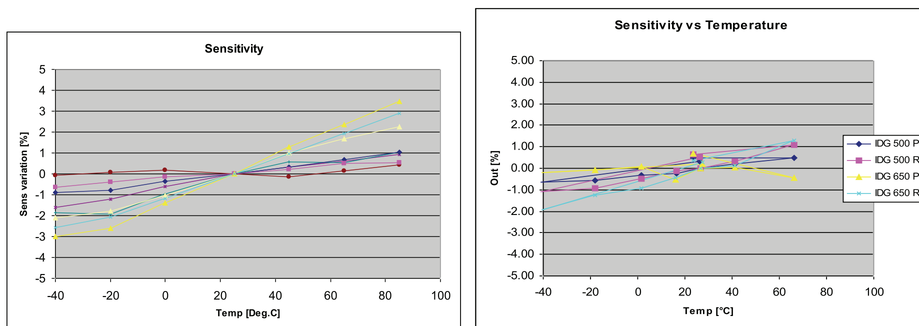

Fig. 13. Scale factor temperature sensitivity test results: STM (left); IS (right).

5.3.4 Frequency response

The sensor frequency response (from the angular rate input to sensor output measurement) has been measured at 16 frequency points, almost regularly spaced in the frequency range $0.1 \div 100\,Hz$. Measurements have been carried out frequency-by-frequency, by evaluating the sensor magnitude and phase responses to an applied sinusoidal angular rate input. As it can be observed in Figs. 14 and 15, the STM and IS sensors have almost identical frequency responses, with a flat magnitude response up to $50\,Hz$ and a phase lag of 45° at $80\,Hz$; the only noticeable difference consists of a flatter magnitude response of the STM sensor at higher frequencies.

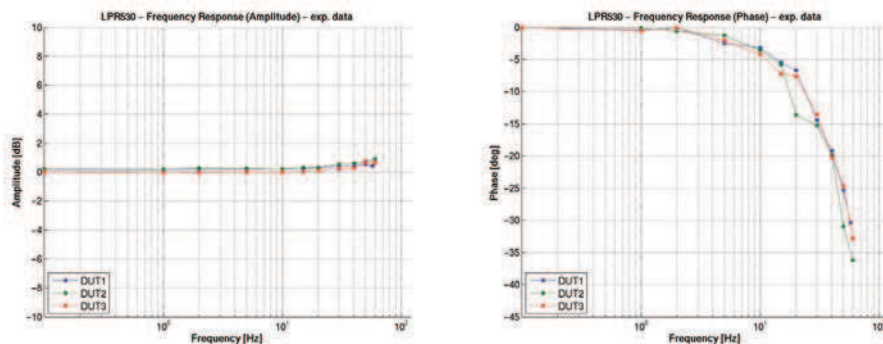

Fig. 14. STM LPR530AL measured frequency response: magnitude (left); phase (right).

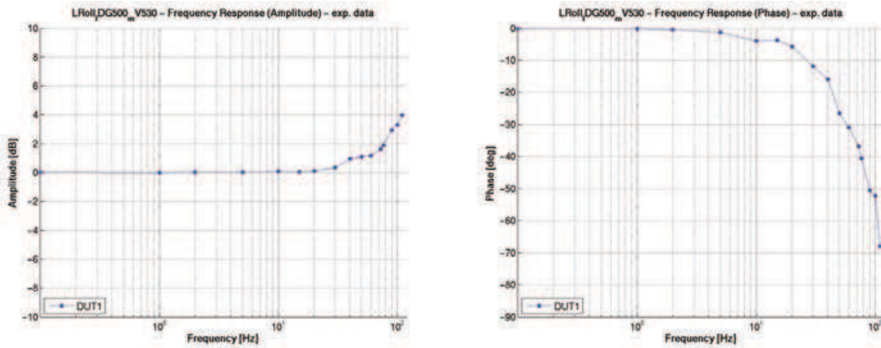

Fig. 15. IS IDG-500/650 measured frequency response: magnitude (left); phase (right).

5.3.5 Noise power spectral density

The output noise Power Spectral Density (PSD) has been measured by using a Digital Signal Analyzer (DSA). For a fair comparison, the full-scales of the two sensors have been selected to be as matched as possible: therefore, the STM sensor FS has been set to $300°/s$ (scale factor $= 3.33\,mV/°/s$), while the IS sensor (IDG-500) FS has been selected as $500°/s$ (scale factor $= 2\,mV/°/s$). With such configuration, the measured output noise floors of the two sensors are almost identical, e.g. $S_n = 0.035\,°/s/\sqrt{Hz}$ for the STM LPR530AL and $S_n = 0.030\,°/s/\sqrt{Hz}$ for the IS IDG-500 (see also Fig. 16).

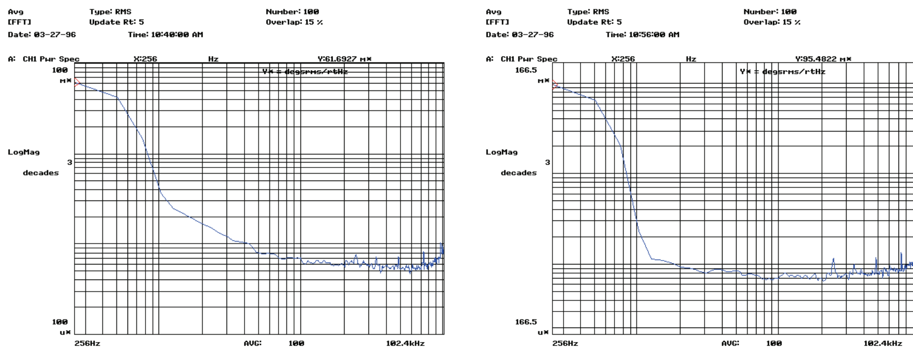

Fig. 16. Output noise power spectral density measurements: STM (left); IS (right).

6. Conclusions

In recent years, the development and commercialization of MEMS gyroscopes have experienced a rapid growth, as a result of performance improvements and cost reductions. Such sensors have begun to be applied in many consumer and industrial applications, either to replace older, bulkier and more expensive angular rate sensors, or to become essential parts in completely new applications requiring small and inexpensive devices.

This paper has provided a brief introduction to the design, technology and industrial requirements aspects behind the recent commercialization of many MEMS gyroscopes for consumer and industrial applications.
In order to assess the performance levels currently achieved by many sensors available in the market, two commercially available sensors, e.g. the STMicroelectronics LPR530AL and the Invensense IDG-500/650 dual-axis pitch & roll MEMS gyroscopes, have been compared by running several benchmark tests. The tests have shown similar results for the two devices, except for the ZRO immunity to mechanical stress, for which the STMicroelectronics sensor has exhibited better performances.
In general, the average performance levels achieved by current MEMS gyroscopes available in the market are sufficient for most of the consumer and industrial applications; nevertheless, it is perhaps only a matter of time before they will become adequate also for the most demanding inertial navigation applications.

7. References

Abe, H., Yoshida, T. & Turuga, K. (1992). Piezoelectric-ceramic cylinder vibratory gyroscope, *Japanese Journal of Applied Physics* 31(Part 1, No. 9B): 3061–3063.

Aerosmith, I. (2005).
URL: *http://www.ideal-aerosmith.com/*

Antonello, R., Oboe, R., Prandi, L., Caminada, C. & Biganzoli, F. (2009). Open loop compensation of the quadrature error in mems vibrating gyroscopes, *Industrial Electronics, 2009. IECON '09. 35th Annual Conference of IEEE*, pp. 4034 –4039.

Apple (2011).
URL: *www.apple.com*

Bernstein, J., Cho, S., King, A., Kourepenis, A., Maciel, P. & Weinberg, M. (1993). A micromachined comb-drive tuning fork rate gyroscope, *Micro Electro Mechanical Systems, 1993, MEMS '93, Proceedings An Investigation of Micro Structures, Sensors, Actuators, Machines and Systems. IEEE.*, pp. 143–148.

Bochobza-Degani, O., Seter, D. J., Socher, E. & Nemirovsky, Y. (2000). A novel micromachined vibrating rate-gyroscope with optical sensing and electrostatic actuation, *Sensors and Actuators A: Physical* 83(1-3): 54 – 60.

Boser, B. (1997). Electronics for micromachined inertial sensors, *Solid State Sensors and Actuators, 1997. TRANSDUCERS '97 Chicago., 1997 International Conference on*, Vol. 2, pp. 1169–1172 vol.2.

Brown, A. (2005). Gps/ins uses low-cost mems imu, *Aerospace and Electronic Systems Magazine, IEEE* 20(9): 3–10.

Bustillo, J., Howe, R. & Muller, R. (1998). Surface micromachining for microelectromechanical systems, *Proceedings of the IEEE* 86(8): 1552–1574.

Chang, S., Chia, M., Castillo-Borelley, P., Higdon, W., Jiang, Q., Johnson, J., Obedier, L., Putty, M., Shi, Q., Sparks, D. & Zarabadi, S. (1998). An electroformed CMOS integrated angular rate sensor, *Sensors and Actuators A: Physical* 66(1-3): 138 – 143.

Clark, W. A., Howe, R. T. & Horowitz, R. (1996). Surface micromachined Z-axis vibratory rate gyroscope, *Tech. Dig. Solid-State Sens. Actuator Workshop, Hilton Head Island*, pp. 283–287.

Damrongsak, B. & Kraft, M. (2005). A micromachined electrostatically suspended gyroscope with digital force feedback, *Sensors, 2005 IEEE*.

Dauwalter, C. & Ha, J. (2005). Magnetically suspended mems spinning wheel gyro, *Aerospace and Electronic Systems Magazine, IEEE* 20(2): 21–26.

Dong, L. & Avanesian, D. (2009). Drive-mode control for vibrational mems gyroscopes, *Industrial Electronics, IEEE Transactions on* 56(4): 956–963.

Dong, Y., Kraft, M., Hedenstierna, N. & Redman-White, W. (2008). Microgyroscope control system using a high-order band-pass continuous-time sigma-delta modulator, *Sensors and Actuators A: Physical* 145-146: 299 – 305.

Drafts, B. (2001). Acoustic wave technology sensors, *Microwave Theory and Techniques, IEEE Transactions on* 49(4): 795–802.

Ellis, C. D. & Wilamowski, B. M. (2008). Fabrication and control of an electrostatically levitated rotating gyro, *in* T. George & Z. Cheng (eds), *Micro (MEMS) and Nanotechnologies for Space, Defense, and Security II*, Vol. 6959, SPIE, p. 69590Q.

Fell, C. (2006). Development of a second generation low cost mems gyroscope: Design for manufacture, *MEMS Sensors and Actuators, 2006. The Institution of Engineering and Technology Seminar on*, pp. 75–82.

Fleming, W. (2001). Overview of automotive sensors, *Sensors Journal, IEEE* 1(4): 296–308.

Geen, J., Sherman, S., Chang, J. & Lewis, S. (2002). Single-chip surface micromachined integrated gyroscope with 50°/h allan deviation, *Solid-State Circuits, IEEE Journal of* 37(12): 1860–1866.

Geiger, W., Folkmer, B., Sobe, U., Sandmaier, H. & Lang, W. (1998). New designs of micromachined vibrating rate gyroscopes with decoupled oscillation modes, *Sensors and Actuators A: Physical* 66(1-3): 118 – 124.

Gupta, P. K. & Jenson, C. E. (1995). Rotation rate sensor with center mounted tuning fork, U.S. Patent 5396144.

Gyration (2009).
URL: *http://www.gyration.com*

Hopkin, I. D., Fell, C. P., Townsend, K. & Mason, T. R. (1999). Vibrating structure gyroscope, U.S. Patent 5932804.

Howe, R. T., Boser, B. E. & Pisano, A. P. (1996). Polysilicon integrated microsystems: technologies and applications, *Sensors and Actuators A: Physical* 56(1-2): 167 – 177.

IEEE Standard for Inertial Sensor Terminology (2001). *IEEE Std 528-2001* .

IEEE Standard Specification Format Guide and Test Procedure for Coriolis Vibratory Gyros (2004). *IEEE Std 1431-2004* .

Invensense (2010).
URL: *http://www.invensense.com/products/idg_650.html*

Jiancheng, F. & Jianli, L. (2009). Integrated model and compensation of thermal errors of silicon microelectromechanical gyroscope, *Instrumentation and Measurement, IEEE Transactions on* 58(9): 2923–2930.

Jose, K. A., Suh, W. D., Xavier, P. B., Varadan, V. K. & Varadan, V. V. (2002). Surface acoustic wave MEMS gyroscope, *Wave Motion* 36(4): 367 – 381.

Juneau, T., Pisano, A. & Smith, J. (1997). Dual axis operation of a micromachined rate gyroscope, *Solid State Sensors and Actuators, 1997. TRANSDUCERS '97 Chicago., 1997 International Conference on*, Vol. 2, pp. 883–886.

Kawano, K., Kobashi, S., Yagi, M., Kondo, K., Yoshiya, S. & Hata, Y. (2007). Analyzing 3d knee kinematics using accelerometers, gyroscopes and magnetometers, *System of Systems Engineering, 2007. SoSE '07. IEEE International Conference on*, pp. 1–6.

Kim, Y. S., Soh, B. S. & Lee, S.-G. (2005). A new wearable input device: Scurry, *Industrial Electronics, IEEE Transactions on* 52(6): 1490–1499.

Knowles, S. J. & Moore, R. H. (2004). Tuning fork with symmetrical mass balancing and reduced quadrature error, U.S. Patent 6701785.

Kotru, S., Zhong, J., Highsmith, A. & Jackson, J. (2008). Design and fabrication of a meso-scale gyroscope, *Microelectronics and Electron Devices, 2008. WMED 2008. IEEE Workshop on*, pp. 5–8.

Kovacs, G., Maluf, N. & Petersen, K. (1998). Bulk micromachining of silicon, *Proceedings of the IEEE* 86(8): 1536–1551.

Kurosawa, M., Fukuda, Y., Takasaki, M. & Higuchi, T. (1998). A surface-acoustic-wave gyro sensor, *Sensors and Actuators A: Physical* 66(1-3): 33 – 39.

Lawrence, A. (1993). *Modern inertial technology - Navigation, guidance, and control*, Springer-Verlag.

Leland, R., Lipkin, Y. & Highsmith, A. (2003). Adaptive oscillator control for a vibrational gyroscope, *American Control Conference, 2003. Proceedings of the 2003*, Vol. 4, pp. 3347 – 3352 vol.4.

Li, X., Bao, M., Yang, H., Shen, S. & Lu, D. (1999). A micromachined piezoresistive angular rate sensor with a composite beam structure, *Sensors and Actuators A: Physical* 72(3): 217 – 223.

Liu, Q. H. & Wu, X. Z. (2007). Design of a Novel MEMS IDT Dual Axes Surface Acoustic Wave Gyroscope, *Nano/Micro Engineered and Molecular Systems, 2007. NEMS '07. 2nd IEEE International Conference on*, pp. 817–820.

Lutz, M., Golderer, W., Gerstenmeier, J., Marek, J., Maihofer, B., Mahler, S., Munzel, H. & Bischof, U. (1997). A precision yaw rate sensor in silicon micromachining, *Solid State Sensors and Actuators, 1997. TRANSDUCERS '97 Chicago., 1997 International Conference on*, Vol. 2, pp. 847–850.

Madni, A., Costlow, L. & Knowles, S. (2003). Common design techniques for BEI GyroChip quartz rate sensors for both automotive and aerospace/defense markets, *Sensors Journal, IEEE* 3(5): 569–578.

Maenaka, K., Fujita, T., Konishi, Y. & Maeda, M. (1996). Analysis of a highly sensitive silicon gyroscope with cantilever beam as vibrating mass, *Sensors and Actuators A: Physical* 54(1-3): 568 – 573.

M'Closkey, R. & Vakakis, A. (1999). Analysis of a microsensor automatic gain control loop, *American Control Conference, 1999. Proceedings of the 1999*, Vol. 5, pp. 3307 –3311 vol.5.

Meirovitch, L. (1970). *Methods of Analytical Dynamics*, McGraw-Hill, New York.

Microstrain (2011).
URL: *http://www.microstrain.com*

Miyazaki, S. (1997). Long-term unrestrained measurement of stride length and walking velocity utilizing a piezoelectric gyroscope, *Biomedical Engineering, IEEE Transactions on* 44(8): 753–759.

muRata (2003).
URL: *http://www.murata.com*

Nalbach, G. (1993). The halteres of the blowfly Calliphora - Part I: kinematics and dynamics, *Journal of Comparative Physiology A: Neuroethology, Sensory, Neural, and Behavioral Physiology* 173(3): 293–300.

Nalbach, G. & Hengstenberg, R. (1994). The halteres of the blowfly Calliphora - Part II: three-dimensional organization of compensatory reactions, *Journal of Comparative Physiology A: Neuroethology, Sensory, Neural, and Behavioral Physiology* 175(6): 695–708.

Nasiri, S. & Flannery Jr., A. F. (2007). Method of making an x-y axis dual-mass tuning fork gyroscope with vertically integrated electronics and wafer-scale hermetic packaging, U.S. Patent 7250112.

Neul, R., Gomez, U.-M., Kehr, K., Bauer, W., Classen, J., Doring, C., Esch, E., Gotz, S., Hauer, J., Kuhlmann, B., Lang, C., Veith, M. & Willig, R. (2007). Micromachined angular rate sensors for automotive applications, *Sensors Journal, IEEE* 7(2): 302–309.

Nintendo (2011).
URL: *http://www.nintendo.com/wii/what/accessories/wiimotionplus*

Nonomura, Y., Fujiyoshi, M., Omura, Y., Fujitsuka, N., Mizuno, K. & Tsukada, K. (2006). Soi rate gyro sensor for automotive control, *Sensors and Actuators A: Physical* 132(1): 42 – 46.

Norgia, M. & Donati, S. (2001). Hybrid opto-mechanical gyroscope with injection-interferometer readout, *Electronics Letters* 37(12): 756–758.

Noureldin, A., Karamat, T., Eberts, M. & El-Shafie, A. (2009). Performance enhancement of mems-based ins/gps integration for low-cost navigation applications, *Vehicular Technology, IEEE Transactions on* 58(3): 1077–1096.

Oboe, R., Antonello, R., Lasalandra, E., Durante, G. & Prandi, L. (2005). Control of a Z-axis MEMS vibrational gyroscope, *Mechatronics, IEEE/ASME Transactions on* 10(4): 364–370.

O'Connor, J. M. & Shupe, D. M. (1983). Vibrating beam rotation sensor, U.S. Patent 4381672.

Painter, C. & Shkel, A. (2003). Active structural error suppression in mems vibratory rate integrating gyroscopes, *Sensors Journal, IEEE* 3(5): 595 – 606.

Paoletti, F., Gretillat, M.-A. & de Rooij, N. (1996). A silicon micromachined vibrating gyroscope with piezoresistive detection and electromagnetic excitation, *Micro Electro Mechanical Systems, 1996, MEMS '96, Proceedings. 'An Investigation of Micro Structures, Sensors, Actuators, Machines and Systems'. IEEE, The Ninth Annual International Workshop on*, pp. 162–167.

Pappas, I., Keller, T., Mangold, S., Popovic, M., Dietz, V. & Morari, M. (2004). A reliable gyroscope-based gait-phase detection sensor embedded in a shoe insole, *Sensors Journal, IEEE* 4(2): 268–274.

Petkov, V. & Boser, B. (2005). A fourth-order ΣΔ interface for micromachined inertial sensors, *Solid-State Circuits, IEEE Journal of* 40(8): 1602 – 1609.

Rajendran, S. & Liew, K. M. (2004). Design and simulation of an angular-rate vibrating microgyroscope, *Sensors and Actuators A: Physical* 116(2): 241 – 256.

Roetenberg, D., Slycke, P. & Veltink, P. (2007). Ambulatory position and orientation tracking fusing magnetic and inertial sensing, *Biomedical Engineering, IEEE Transactions on* 54(5): 883–890.

R.R.Ragan (ed) (1984). Inertial technology for the future, *Aerospace and Electronic Systems, IEEE Transactions on* AES-20(4): 414–444.

Sachs, D., Nasiri, S. & Goehl, D. (n.d.). Image stabilization technology overview. Available at: http://www.invensense.com/cn/shared/pdf/ImageStabilizationWhitepaper_051606.pdf.

Saukoski, M., Aaltonen, L. & Halonen, K. (2007). Zero-rate output and quadrature compensation in vibratory mems gyroscopes, *Sensors Journal, IEEE* 7(12): 1639–1652.

Segway (2011).
URL: *http://www.segway.com*

Seidel, H., Aikele, M., Rose, M. & Toelg, S. (2002). Safety relevant microsystems for automotive applications, *Microsystem Technologies* 7(5): 244–248.

Senturia, S. D. (2001). *Microsystem Design*, Kluwer Academic Publishers.

Shakoor, R. I., Bazaz, S. A., Kraft, M., Lai, Y. & ul Hassan, M. M. (2009). Thermal Actuation Based 3-DoF Non-Resonant Microgyroscope Using MetalMUMPs, *Sensors* 9(4): 2389–2414.

Shearwood, C., Ho, K. Y., Williams, C. B. & Gong, H. (2000). Development of a levitated micromotor for application as a gyroscope, *Sensors and Actuators A: Physical* 83(1-3): 85 – 92.

Soderkvist, J. (1991). Piezoelectric beams and vibrating angular rate sensors, *Ultrasonics, Ferroelectrics and Frequency Control, IEEE Transactions on* 38(3): 271–280.

Söderkvist, J. (1994). Micromachined gyroscopes, *Sensors and Actuators A: Physical* 43(1-3): 65 – 71.

Sparks, D., Zarabadi, S., Johnson, J., Jiang, Q., Chia, M., Larsen, O., Higdon, W. & Castillo-Borelley, P. (1997). A CMOS integrated surface micromachined angular rate sensor: it's automotive applications, *Solid State Sensors and Actuators, 1997. TRANSDUCERS '97 Chicago., 1997 International Conference on*, Vol. 2, pp. 851–854 vol.2.

Stewart, R. E. (2009). Micro hemispheric resonator gyro, U.S. Patent 2009/0031831.

STMicroelectronics (2010).
URL: *http://www.st.com/stonline/products/literature/ds/15812/lpr530al.pdf*

Stringer, J. (2000). *The Air Force Institute of Technology (AFIT) Micro Electro-Mechanical Systems (MEMS) Interferometric Gyroscope (MiG)*, Master's thesis, Air Force Institute of Technology (AFIT).

Tanaka, K., Mochida, Y., Sugimoto, M., Moriya, K., Hasegawa, T., Atsuchi, K. & Ohwada, K. (1995). A micromachined vibrating gyroscope, *Sensors and Actuators A: Physical* 50(1-2): 111 – 115.

Tang, W., Nguyen, T.-C. & Howe, R. (1989). Laterally driven polysilicon resonant microstructures, *Micro Electro Mechanical Systems, 1989, Proceedings, An Investigation of Micro Structures, Sensors, Actuators, Machines and Robots. IEEE*, pp. 53–59.

Tsai, N.-C., Huang, W.-M. & Chiang, C.-W. (2009). Magnetic actuator design for single-axis micro-gyroscopes, *Microsystem Technologies* 15(4): 493–503.

Vellekoop, M. J. (1998). Acoustic wave sensors and their technology, *Ultrasonics* 36(1-5): 7 – 14. Ultrasonics International 1997.

Voss, R., Bauer, K., Ficker, W., Gleissner, T., Kupke, W., Rose, M., Sassen, S., Schalk, J., Seidel, H. & Stenzel, E. (1997). Silicon angular rate sensor for automotive applications with piezoelectric drive and piezoresistive read-out, *Solid State Sensors and Actuators, 1997. TRANSDUCERS '97 Chicago., 1997 International Conference on*, Vol. 2, pp. 879–882 vol.2.

Weinberg, M. & Kourepenis, A. (2006). Error sources in in-plane silicon tuning-fork MEMS gyroscopes, *Microelectromechanical Systems, Journal of* 15(3): 479–491.

Yazdi, N., Ayazi, F. & Najafi, K. (1998). Micromachined inertial sensors, *Proceedings of the IEEE* 86(8): 1640–1659.

Yokota, S., Imamura, T., Takemura, K., Edamura, K. & Kumagai, H. (2008). A liquid rate gyroscope using electro-conjugate fluid, *Intelligent Sensors, Sensor Networks and Information Processing, 2008. ISSNIP 2008. International Conference on*, pp. 459–464.

Zhou, J., Yan, G., Zhu, Y., Xiao, Z. & Fan, J. (2005). Design and fabrication of a microfluid angular rate sensor, *Micro Electro Mechanical Systems, 2005. MEMS 2005. 18th IEEE International Conference on*, pp. 363–366.

Zhu, R., Ding, H., Su, Y. & Zhou, Z. (2006). Micromachined gas inertial sensor based on convection heat transfer, *Sensors and Actuators A: Physical* 130-131: 68 – 74.

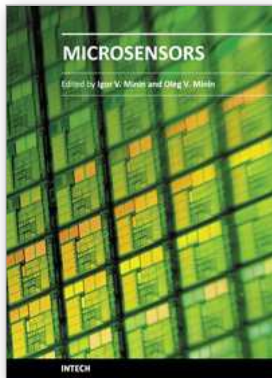

Microsensors

Edited by Prof. Igor Minin

ISBN 978-953-307-170-1
Hard cover, 294 pages
Publisher InTech
Published online 09, June, 2011
Published in print edition June, 2011

This book is planned to publish with an objective to provide a state-of-art reference book in the area of microsensors for engineers, scientists, applied physicists and post-graduate students. Also the aim of the book is the continuous and timely dissemination of new and innovative research and developments in microsensors. This reference book is a collection of 13 chapters characterized in 4 parts: magnetic sensors, chemical, optical microsensors and applications. This book provides an overview of resonant magnetic field microsensors based on MEMS, optical microsensors, the main design and fabrication problems of miniature sensors of physical, chemical and biochemical microsensors, chemical microsensors with ordered nanostructures, surface-enhanced Raman scattering microsensors based on hybrid nanoparticles, etc. Several interesting applications area are also discusses in the book like MEMS gyroscopes for consumer and industrial applications, microsensors for non invasive imaging in experimental biology, a heat flux microsensor for direct measurements in plasma surface interactions and so on.

How to reference

In order to correctly reference this scholarly work, feel free to copy and paste the following:

Riccardo Antonello and Roberto Oboe (2011). MEMS Gyroscopes for Consumers and Industrial Applications, Microsensors, Prof. Igor Minin (Ed.), ISBN: 978-953-307-170-1, InTech, Available from: http://www.intechopen.com/books/microsensors/mems-gyroscopes-for-consumers-and-industrial-applications

INTECH
open science | open minds

InTech Europe
University Campus STeP Ri
Slavka Krautzeka 83/A
51000 Rijeka, Croatia
Phone: +385 (51) 770 447
Fax: +385 (51) 686 166
www.intechopen.com

InTech China
Unit 405, Office Block, Hotel Equatorial Shanghai
No.65, Yan An Road (West), Shanghai, 200040, China
中国上海市延安西路65号上海国际贵都大饭店办公楼405单元
Phone: +86-21-62489820
Fax: +86-21-62489821

© 2011 The Author(s). Licensee IntechOpen. This chapter is distributed under the terms of the Creative Commons Attribution-NonCommercial-ShareAlike-3.0 License, which permits use, distribution and reproduction for non-commercial purposes, provided the original is properly cited and derivative works building on this content are distributed under the same license.